JOURNAL OF MATERIALS SCIENCE 30 (1995) 2656–2667

Strength characterization of yttria-partially stabilized zirconia

R. K. GOVILA
Material Systems Reliability Department, Scientific Research Laboratory, MD No. 2313, Ford Motor Company, P.O. Box 2053, Dearborn, MI 48121-2053, USA

The flexural strength of yttria-partially stabilized zirconia was evaluated as a function of temperature (20–1000 °C in air), applied stress and time. The material was susceptible to strength degradation at low temperatures (200 and 300 °C) due to the phase transformation of the tetragonal structure to monoclinic, possibly accompanied by microcracking. In this temperature range, the material was incapable of sustaining low applied stress levels of 276 MPa for any significant duration (> 100 h < 500 h). Stress rupture testing at 600 °C and above identified the onset of viscous flow of the glassy phase and consequent degradation of material strength.

1. Introduction

During the last twenty years, a variety of high performance ceramic materials, such as silicon nitrides and carbides, sialons, whisker-reinforced ceramic composites and partially stabilized zirconia (PSZ) have been developed for use as structural components in heat engine applications. Among these ceramics, PSZ is of special interest due to its high strength and toughness. The use of PSZ materials for insulation and structural components in adiabatic diesel engines [1–4] and other types of industrial applications [5–15] is being investigated. The primary reasons for PSZ use in diesel engine applications are low thermal conductivity (good insulation), high coefficient of thermal expansion (close to cast iron and steel), good oxidation and thermal shock resistance. In general, PSZ usually consists of two or more phases (cubic, tetragonal and monoclinic). The good mechanical properties (bend strength of ≥ 1000 MPa and toughness of ≥ 10 MPa $m^{1/2}$ at 20 °C) of PSZ ceramics are primarily a result of a stress induced "martensitic" phase transformation of the metastable tetragonal phase to the stable monoclinic phase, hence the name "transformation toughening". The Y_2O_3 or CeO_2–PSZ can be controlled to contain almost 100% tetragonal zirconia phase [16–21] of submicrometre grain size. These materials are often referred to as "tetragonal zirconia polycrystal" or TZP and have been reviewed by Nettleship and Stevens [22].

Yttria containing tetragonal zirconia (Y–PSZ or Y–TZP) in the sintered state has been studied by several investigators [16–19, 22–38] and bend strengths of the order of 1000 MPa at room temperature are attainable. Several types of processing, fabrication and material (powder impurity) related strength controlling defects [37–40] have been identified in these materials. In general, it appears that in sintered ceramic materials the presence of porosity or porous regions may be the major strength controlling defect. If Y–PSZ/TZP is to be used for ceramic structural components in engine applications, where temperatures of the order of 200–1000 °C can easily be attained, it is necessary to characterize the strength behaviour in detail, especially the long term reliability and durability at temperatures of interest.

This study was undertaken to characterize the strength of a commercially available sintered Y–PSZ/TZP material by evaluating the fracture strength as a function of temperature (20–1000 °C in air); failure initiation sites and the mode of crack propagation were also examined. Long term reliability and durability were evaluated using flexural stress rupture testing at several temperatures. In addition, detailed X-ray diffraction analysis of the test samples was done in order to determine the various phases produced due to the combined effects of intermediate temperature (200–600 °C) and stress induced transformation, and the resulting influence on strength and failure was investigated.

2. Experimental procedure

2.1. Material and fabrication

The material used in this study was a sintered yttria-partially stabilized zirconia commercially known as NGK Locke Z-191. The material was obtained in the form of a hollow cylinder (length 138 mm, inside and outside diameters 80 and 100 mm, respectively). The exact chemical composition and sintering parameters (time, temperature, pressure and environment) are not known due to the proprietary nature of this material. However, it is believed that the Y–PSZ (Z-191) contained 3 mol % yttria as stabilizer [38] and small amounts of silica as powder impurity.

0022–2461

2.2. Specimen preparation and testing (fast fracture and stress rupture)

Flexural test specimens (approximately 32 mm long × 6 mm wide × 3 mm thick) were machined from the hollow cylinder (test component) wall. All faces were ground lengthwise using 320 grit diamond wheels; the edges were chamfered lengthwise to prevent notch effects. All specimens were tested in the as-machined condition, and no further surface polishing or any heat treatment was carried out prior to testing.

For flexural strength evaluation, specimens were tested in one-quarter-point, four-point bending (inner span is one-half of the outer span) in an Instron testing machine (model 1125) using a specially designed self-aligning ceramic fixture [41] made from hot pressed SiC. The outer and inner knife edges of the testing fixture were spaced approximately 19 and 9.5 mm apart, respectively. The high temperature bend tests were conducted in air using a rapid temperature response furnace attached to the testing machine head. In high temperature tests, specimens were held at the test temperature for 15 min to achieve thermal equilibrium before testing was begun. No preload was applied on test specimens for either room temperature or high temperature tests. All specimens were tested at a machine crosshead speed (MCS) of $0.5\,mm\,min^{-1}$.

The flexural stress rupture tests at elevated temperatures (200–1000 °C) in air environment were also conducted in four-point bending using the self-aligning ceramic fixture and furnace. The load was applied to the test specimen through a lever arm, dead weight type assembly. The experimental set-up was equipped with a microswitch to cut off power to the furnace and the timer at the instant specimen failure occurred. The total time to failure was recorded.

The tensile surface of flexural specimens in the as-machined state (except one specimen was annealed at 1038 °C in air for 24 h) was used for taking X-ray diffraction using CuK_α radiation for 2θ between 24–38° ([37–39] to determine the presence of tetragonal, monoclinic and cubic zirconia phases. Two flexural specimens were polished to 1 μm finish, thermally etched at 1400 °C for 1 h in air, and examined in a scanning electron microscope (SEM) in order to reveal the grain size and grain morphology of the tetragonal zirconia phase (matrix) and to identify the presence of any other powder impurities. A surface profilometer was used to measure the maximum deflection observed in stress rupture specimens which sustained the applied stress for over 100 h and did not fail.

Fracture surfaces of selected specimens were examined in SEM using both secondary electron image (SEI) and back scattered electron image (BSEI) for surface topography and chemical composition. In addition, elemental distribution or X-ray mapping was done in the SEM with energy dispersive spectroscopy. Complete experimental details of flexural strength evaluation (in a fast fracture mode, MCS = $0.5\,mm\,min^{-1}$) at room temperature and above (300–1000 °C), flexural stress rupture testing at elevated temperatures (200–1000 °C) in an air environment and self-aligning ceramic test fixture have been reported previously [41–43].

3. Results and discussion

3.1. Microstructure and phases

The X-ray diffraction patterns taken from the tensile surface of specimens in the as-machined and annealed at 1038 °C for 24 h in air are shown in Fig. 1a, b, respectively. The diffraction pattern taken from a specimen tested in four-point bending at 20 °C was similar to that seen in Fig. 1a. The diffraction pattern, Fig. 1a, indicated the presence of cubic (c), tetragonal (t) and monoclinic (m) zirconia phases. The cubic and tetragonal lines overlap each other, but microstructural examination helped in revealing and possibly identifying, as shown below, that the matrix was primarily made up of t-phase, c-phase and possibly traces of m-phase. The small presence of the m-phase in the as-machined condition, Fig. 1a, is believed to be due to surface machining of the specimen which transforms the t-phase to m-phase, and disappears almost completely upon annealing the specimen at 1038 °C, Fig. 1b, as suggested by Cassidy *et al.* [44] and discussed later. The diffraction pattern also confirmed the presence of a relatively small amount of silica (SiO_2) in the Y–PSZ matrix. The volume fractions of the various zirconia phases present in the material (Z-191) have been determined earlier by others [37, 38] and, therefore, no such measurements were made in this study.

The microstructure of the sintered Y–PSZ is shown in Fig. 2; the matrix is primarily composed of small t-phase grains, and it is believed that the large grains seen are of c-phase. The grain size of the t-phase varied from 0.18 to 0.35 μm and that of the c-phase varied from 1 to 3 μm. The m-phase grains are indistinguishable microstructurally because of their similar size to the t-grains, and can only be identified either by X-ray diffraction, as shown in Fig. 1, or by transmission electron microscopy. Thermal etching (1400 °C for 1 h in air) of the specimen caused melting of the crystalline glassy phase silica (SiO_2) and left a very thin film over the entire polished surface of the specimen. In addition, pockets of glassy phase silica inhomogeneously distributed in the matrix appeared, as shown in Fig. 2, as dark coloured regions, marked 2. Energy dispersive X-ray spectra of region 2 confirmed the localized concentration of element Si and the presence of element Zr due to the surrounding matrix. Energy dispersive X-ray spectra taken outside region 2 showed a significantly decreased amount of the element Si. This inhomogeneous distribution of silica was confirmed on the fracture face of specimens tested at 20 °C, as shown later. It should be pointed out that the strength of the Y–PSZ greatly depends on the amount and the grain size of the various zirconia phases present in the matrix [26, 29]. The fine grained t-phase is the strongest and the large grained c-phase is the weakest [29].

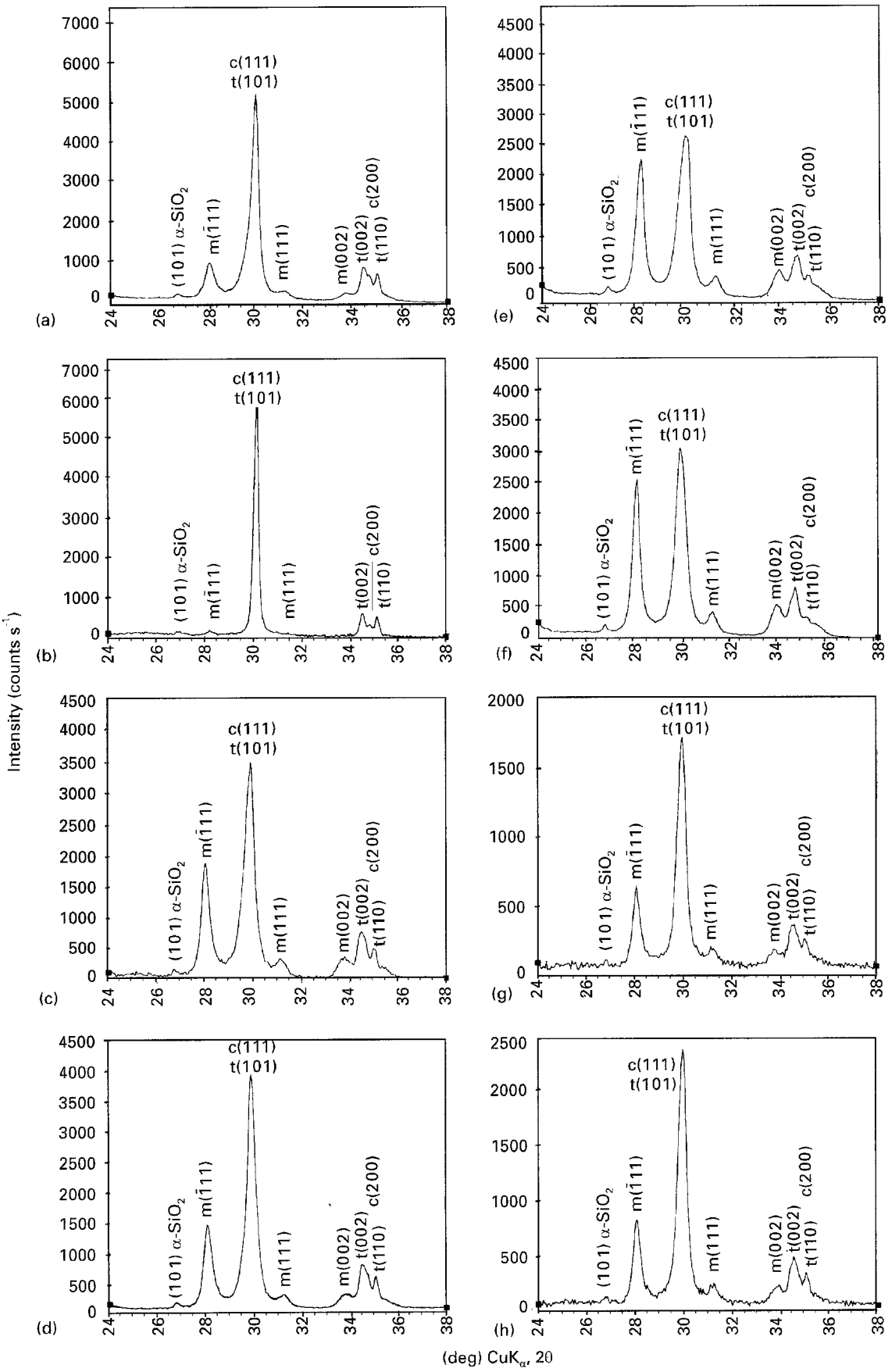

Figure 1 X-ray diffraction patterns of Y–PSZ/TZP material: (a) sintered Y–PSZ as-machined (NGK–Z–191); (b) annealed at 1038 °C for 24 h; (c) at 200 °C, 276 MPa, failed at 206 h; (d) at 200 °C, 413 MPa, failed at 142 h; (e) at 300 °C, 276 MPa, failed at 30 h; (f) at 400 °C, 276 MPa, failed at 305 h; (g) at 600 °C, 344 MPa, failed at 153 h; and (h) at 600 °C, 413 MPa, failed at 10 h.

3.2. Flexural strength versus temperature

At room temperature (20 °C), a total of ten specimens were tested in four-point bending to determine the fast fracture strength. A typical statistical variation in fracture strength, σ_F, at 20 °C is shown in Fig. 3. The σ_F varied from a minimum of 865 MPa to a maximum of 1207 MPa, with a Weibull characteristic strength of 1121 MPa, an average strength of 1077 MPa,

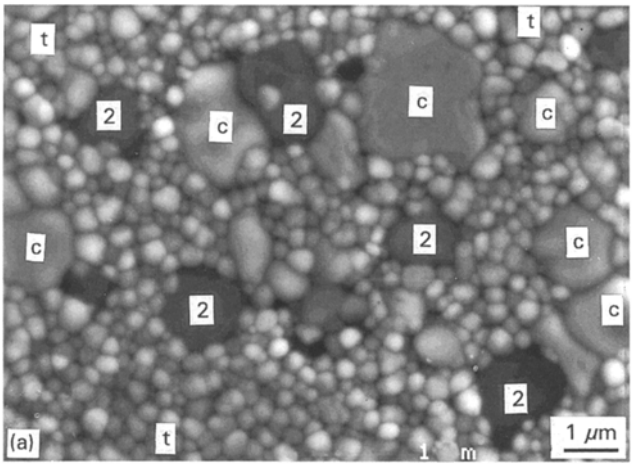

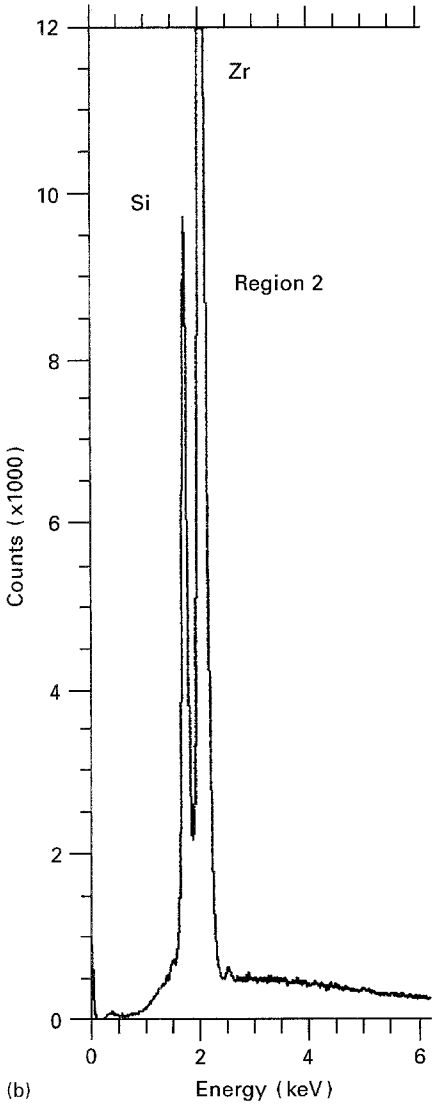

Figure 2 (a) Typical microstructure of Y–PSZ/TZP (NGK–Z-191) as revealed in SEM (SE-I) showing distribution of tetragonal (t) and cubic (c) phase zirconia grains. (b) Energy dispersive X-ray spectra taken in region 2 showed the presence of Si.

a Weibull modulus of 12, and a standard deviation of 108 MPa. These strength values are slightly different from those reported by the manufacturer [45] and others [26, 38, 46–49]. The differences in strength and modulus data may be partly due to a small number of specimens tested in this study, variations in specimen geometry and test span dimensions, and compositional differences in the as-received material due to

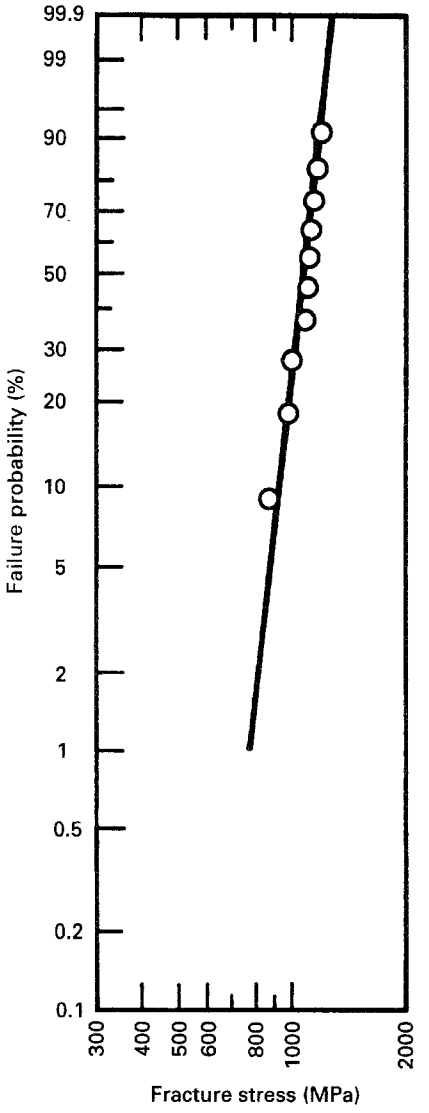

Figure 3 Statistical variation in four-point bending fracture strength for Y–PSZ/TZP (NGK–Z-191) at 20 °C. Average strength = 1077 MPa, standard deviation = 108 MPa, m = 12.

fabrication, such as billets used in other studies and cylinder liners in this study. The load–deflection curves for specimens tested at 20 °C displayed non-linear (deviation from the elastic line) behaviour similar to that observed in MgO–PSZ by Marshall [50] due to stress induced transformation of the t-phase to m-phase during testing that disappeared at higher temperatures.

Examination of the fracture surfaces in all specimens tested at 20 °C revealed that the majority of failures initiated either at a surface or subsurface porous region. In several specimens, the failure initiating porous region displayed the presence of glassy phase silica (SiO_2). The presence of large c-phase zirconia grains as the failure initiation source was also seen in some specimens (see Tables I and II, and Fig. 10). A typical example of a surface initiated failure is shown in Fig. 4a. At this stage of examination, it is difficult to distinguish the presence of any impurity associated with the failure region. However, examination of the same region as seen in Fig. 4a in back scattered electron image (BSEI) mode, Fig. 4b, revealed that the chemical composition of the failure origin was different from that of the surrounding

TABLE I Fast fracture strength data for sintered yttria-partially stabilized zirconia (Z-191)

Test no.	Test temperature (°C)	Fracture strength (MPa)	Fracture origin
1	20	865	Surface initiated porous region, presence of Si
2		1207	Surface initiated porous region, presence of Si, Fig. 4
3		1120	Subsurface porous region
4		1170	Subsurface porous region
5		1163	Surface initiated porous region
6		1104	Surface initiated porous region
7		988	Subsurface porous region
8		966	Surface initiated large cubic zirconia grains
9		1120	Surface initiated porous region
10		1071	Surface initiated porous region
11	300	1048	Corner failure, large cubic zirconia grians
12		1098	Corner failure
13		604	Corner failure
14	400	1049	Corner failure
15		680	Surface initiated porous region
16		1010	Surface initiated porous region
17		828	Porous region near corner
18		735	Subsurface porous region
19	600	796	Subsurface porous region
20		828	Surface initiated porous region
21		621	Subsurface porous region
22		889	Subsurface porous region
23		733	Surface initiated porous region
24	800	598	Subsurface porous region
25		485	Surface initiated porous region
26		608	Subsurface porous region
27		555	Subsurface porous region
28		586	Subsurface porous region
29	1000	386	Subsurface porous region, presence of Si
30		417	Subsurface porous region

TABLE II Flexural stress rupture results for sintered yttria-partially stabilized zirconia (Z–191)

Test no.	Test temperature[a] (°C)	Applied stress (MPa)	Failure time (h)	Sustained time without failure	Remarks
1	20	482	–	260	No bending
2	200	276	206[b]	–	Fine bending, Fig. 6
3		413	142[b]	–	Bending, Fig. 6
4	300	276	30[b]	–	No bending, corner failure
5		276	26[b]	–	No bending, corner failure
6		276	21[b]	–	No bending, corner failure
7		276	18[b]	–	No bending, corner failure
8		276	22[b]	–	No bending, corner failure
9		276	25[b]	–	No bending, corner failure
10		344	10[b]	–	No bending, corner failure
11		344	23[b]	–	No bending, corner failure
12		413	12[b]	–	No bending, corner failure
13		413	15	–	No bending, corner failure, Fig. 7
14	400	276	–	305	Bending (maximum deflection = 14 μm)
15		344	–	310	Bending (maximum deflection = 110 μm), Fig. 6
16	600	344	153	–	Corner failure, SCG, Fig. 8
17		413	3	–	No bending, SCG, Fig. 9
18		413	10	–	No bending, SCG, Fig. 10
19		413	–	259	No bending
20		413	–	315	No bending
21	800	344	5	–	No bending, failed at the outer loading edge
22		344	–	215	Bending (maximum deflection = 5 μm)
23		344	–	237	Bending (maximum deflection = 6 μm)
24		413	11[b]	–	No bending, corner failure
25		413	–	260	Bending (maximum deflection = 8 μm)
26	1000	276	2	–	No bending, porous region
27		344	0	–	Instant failure, subsurface large porous region

[a] As machined specimens were white in colour. All specimens tested above room temperature showed discolouration (off-white).
[b] Fracture surface did not clearly display the failure origin site, but the direction of river lines (characteristic of crack propagation) suggested corner associated failure.

matrix. The energy dispersive X-ray spectra taken from regions marked 1 and 2, and shown in Fig. 4d, clearly identified the presence of elemental Si in region 1 (failure region) and the absence of Si in region 2 (the matrix). The matrix microstructure, showing the equiaxed fine grained t-phase grains and the much larger c-phase grains (indicated by C) is shown in Fig. 4c. From the fractographs shown in Fig. 4, and examination of the fracture surfaces of other specimens tested at 20 °C (Table I), it appeared that the primary mode of crack propagation during fast fracture (MCS = 0.5 mm min^{-1}) was primarily transgranular. At 20 °C, the failure initiating flaws varied in size from 30 to 80 μm, and the matrix microstructure showed considerable variation in the volume fraction of c-phase present from specimen-to-specimen.

The identification of silicon is associated with small amounts of silica (SiO_2) present as an impurity in the powder. The presence of SiO_2 is beneficial in producing improved densification of the ceramic via liquid phase sintering, and detrimental in degrading the mechanical strength both at 20 °C and higher temperatures, due to its presence as a grain boundary glassy phase, as discussed in detail by Mecartney [51]. Recently, Drennan and Hannink [52] have pointed out the benefits of small additions of strontia (SrO) to MgO–PSZ in reducing the deleterious effects of SiO_2. It appears that Y–PSZ/TZP (Z-191) can be fabricated as large components, and the flexural strength can be further improved by optimizing the sintering additives and conditions, and minimizing the presence of oxide impurities.

Flexural strength was also evaluated at higher temperatures (300–1000 °C), and the variation in σ_F as a function of temperature for fast fracture (MCS = 0.5 mm min^{-1}) is shown in Fig. 5. A continuous decrease in σ_F with increasing temperature is clearly visible in Fig. 5, which is due to the decreased extent of stress induced martensitic phase transformation of the t-phase to m-phase. This behaviour increases with increasing temperature, hence the decreased fracture strength. The large scatter in σ_F values, especially in tests at low and intermediate temperatures (300, 400 and 600 °C) as shown, Fig. 5, may be associated with the low temperature strength degradation phenomenon commonly observed in Y–PSZ/TZP materials. A spontaneous transformation of the t-grains to m-grains occurs, accompanied by micro and macrocracking along grain boundaries, as discussed in detail in the next section. Examination of the fracture surface and the tensile surface of all specimens shown in Fig. 5, failed to reveal the formation of such microcracks. In addition, X-ray diffraction of the failed specimens did not show significant increase in the presence of the m-phase compared to that seen in Fig. 1a, suggesting that failure was not due to m-phase formation. The load–deflection curves during fast loading (MCS = 0.5 mm min^{-1}) at higher

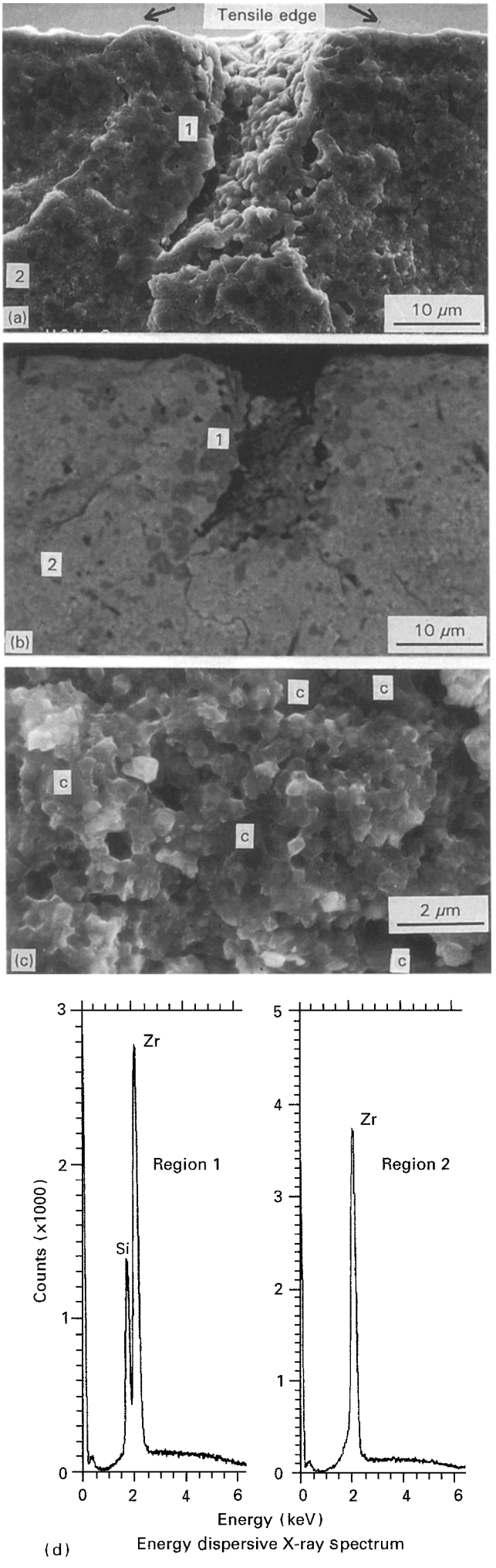

Figure 4 SEM fractographs showing typical surface initiated failure in Y–PSZ/TZP (NGK–Z-191): (a) at 20 °C, 1207 MPa; (b) back scattered mode composition, (c) region 2; and (d) spectra for regions 1 and 2.

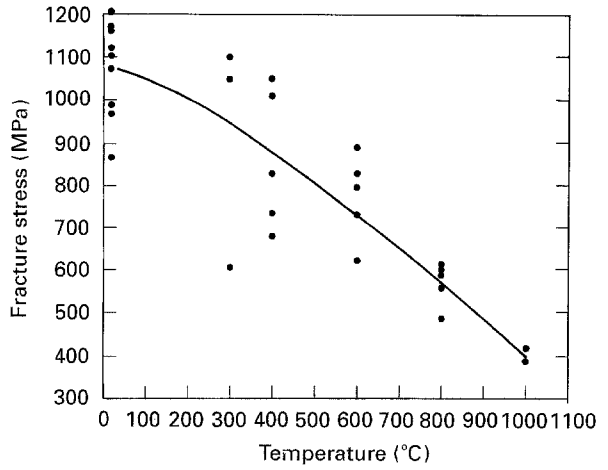

Figure 5 Variation in fast fracture strength of Y–PSZ/TZP (NGK/Z-191) as a function of temperature. All specimens were tested at a machine crosshead speed of 0.5 mm min^{-1}. Complete strength data are given in Table I.

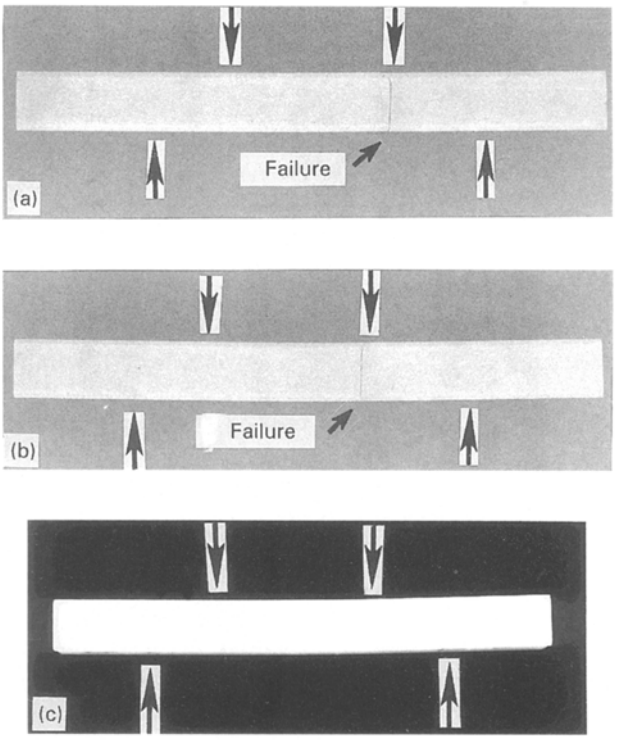

Figure 6 Overall view of the flexural specimens (NGK–Z-191) tested in stress rupture mode showing bending and failure: (a) at 200 °C, 276 MPa, failing at 206 h; (b) at 200 °C, 413 MPa, failing at 142 h; and (c) at 400 °C; 344 MPa, specimen sustained at 310 h.

temperatures up to 1000 °C, showed completely linear elastic behaviour due to the absence of macroscale creep deformation associated with the presence of SiO_2. In addition, fractured specimens did not show any bending, nor the formation of slow crack growth (SCG) regions. Failure origins on the fracture surface were similar to those seen in tests made at 20 °C, further confirming the absence of creep deformation. However, the decrease in strength at 600 °C and above is believed to be a result of the onset of subcritical crack growth or SCG due to the softening of glassy phase silica (SiO_2) distributed along grain boundaries. This was confirmed in flexural stress rupture testing as discussed next.

3.3. Flexural stress rupture

Several studies [53–63] have clearly shown that Y–PSZ/TZP is susceptible to strength degradation during relatively low temperature (150–400 °C) ageing. The degradation is primarily due to phase transformation of the tetragonal structure to monoclinic, accompanied by micro and macrocracking, the severity of which increases between 200 and 300 °C, and in the presence of moisture. Reducing the grain size (0.15–0.30 μm) of the tetragonal structure, or increasing the content of Y_2O_3 stabilizes the tetragonal phase and, thereby, decreases the tendency for strength degradation. Recently, Cassidy *et al.* [44] showed that minor modifications in the sintering cycle, such as from the usual 24 h at 1450 °C to 30 min to 4 h at 1400 or 1450 °C, followed sintering with a 24 h anneal at 1038 °C, resulted in no degradation in flexural strength of 3Y–TZP after ageing at 250 °C for long periods (180 days). This proposed sintering and annealing treatment appears to remove all detectable traces of pre-existing m-phase in the Y–PSZ/TZP, and prevents further formation during ageing at low temperatures. However, the validity of this proposal has yet to be confirmed! Flexural stress rupture tests were carried out as a function of temperature (20–1000 °C) and applied stress, in order to

1. determine the material's susceptibility for low temperature instability,
2. determine the presence of SCG, and
3. identify allowable stress levels for a limited time ($\leq$ 500 h).

In all, 27 specimens were tested in the stress rupture mode, and the results are summarized in Table II.

At 20 °C, one specimen immersed in water during the entire testing period was tested at an applied stress of 482 MPa, and sustained the stress for 260 h without showing failure or bending. The tensile surface of the test specimen was examined by X-ray diffraction to detect the presence of the m-phase. The amount of m-phase present in this specimen was slightly greater than that seen in the as-machined sample, Fig. 1a, but perhaps not large enough to nucleate microcracks of critical size to cause failure.

At 200 °C, two specimens were tested at applied stresses of 276 and 413 MPa, and failed after 206 and 142 h, respectively. Both specimens displayed bending, Fig. 6. Similar creep deformation has been observed in Y–PSZ/TZP by others [26, 29]. Examination of the fracture surfaces failed to reveal the failure initiation sites in both specimens. X-ray diffraction taken from the tensile surface* of the fractured specimens are

* Ideally, the X-ray diffraction should be taken from the fracture face, preferably from the failure initiation region. This would require the use of a 'microfocus X-ray beam camera' to obtain a diffraction pattern, and such equipment is not currently used in our laboratory. Also, the cross-sectional area of the fracture surface is relatively small compared to the surface area of the tensile surface of the failed specimen.

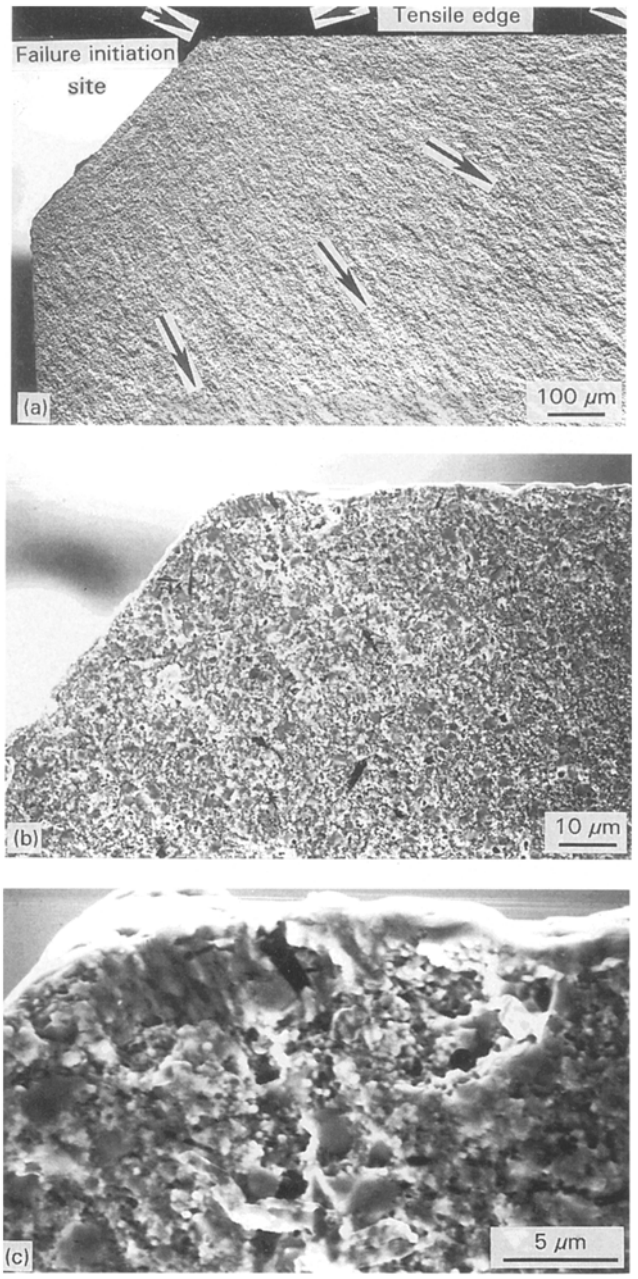

Figure 7 SEM fractographs showing failure initiation and propagation in a Y–PSZ/TZP (NGK–Z-191) specimen tested in stress rupture: (a) topography in back scattered mode at 300 °C, 413 MPa, failure at 15 h, (b) showing failure region, (c) showing failure origin.

shown in Fig. 1c, d, and clearly show significant m-phase formation relative to the as-machined specimen, Fig. 1a. During the tetragonal-to-monoclinic transformation, an increase in volume of 4 to 5% occurs and, therefore, the bending of specimens or creep deformation occurred in order to accommodate the volume increase.

At 300 °C, six specimens were tested at an applied stress of 276 MPa, and all failed in periods ranging from 18 to 30 h. As the applied stress was increased to 344 and 413 MPa, the time-to-failure decreased, ranging from 10 to 23 h, Table II. X-ray diffractions taken from the tensile surface of all fractured specimens revealed significant amounts of m-phase formation relative to the as-machined specimen, as typically shown in Fig. 1e. Examination of the fracture surfaces in the majority of the specimens (nine out of ten, Table II) did not show clearly any "zones of monoclinic phase formation" or micro and macrocrack initiations, as observed by Swab [63] and others [26, 29] in other Y–PSZ compositions. However, the failure appeared to be initiated near the corner of the specimen, as typically shown in Fig. 7. The low magnification view taken in BSEI mode, Fig. 7a, clearly indicates that failure initiated near the corner. The failure region is shown in Fig. 7b, and does not show the presence of any porosity, inclusion or large (1–3 μm size) c-phase grains as a source of failure origin. However, examination of the failure region area, near the corner at the tensile edge side at a higher magnification, Fig. 7c, revealed grain boundary cracking, cavitation and microcracking causing separation of the equiaxed fine grained structure. It is hypothesized that this may be the "stress-induced transformation" area, where m-phase formation occurred together with microcracking. The m-phase grains are essentially of the same size as the original t-grains, and the accompanying microcracks that formed during the transformation are about 1–3 μm long. In this localized region, Fig. 7c, crack propagation was intergranular. It is important to point out that a large number of specimens tested at this temperature failed from the corner, suggesting the possibility of machining damage. Prior to testing, all specimens were examined in an optical microscope at ×25 in order to detect any machining damage, and only those specimens were used which were free from any macro damage. In short, the fact that repeated failures occurred at low applied stress levels and showed extensive m-phase formation strongly suggests that failure was a result of the t-phase transformation.

At 400 °C, the first specimen (No. 14, Table II) tested at an applied stress of 276 MPa did not fail, sustaining the stress for 305 h and displaying minor bending. X-ray diffraction taken from the tensile surface of this specimen is shown in Fig. 1f, and the amount of m-phase formation in this specimen is about the same as that observed in specimens tested at 300 °C, Fig. 1e. Another specimen (No. 15, Table II) tested at an increased applied stress level of 344 MPa did not fail, sustaining the stress for 310 h and displaying bending, Fig. 6. X-ray diffraction of this specimen was similar to that seen earlier, Fig. 1f.

As the testing temperature increased to 600 °C, the material showed a distinctly different behaviour to that seen earlier at 200 and 300 °C. It appears that the influence of the presence of the grain boundary glassy phase silica (SiO_2) became more pronounced, and fracture surfaces of test specimens showed SCG regions. At an applied stress of 344 MPa and a temperature of 600 °C, failure occurred in 153 h, Fig. 8. X-ray diffraction taken from the tensile surface of the fractured specimen is shown in Fig. 1g. The amount of m-phase formation is clearly much less than that seen at 300 and 400 °C, Fig. 1e, f, but considerably greater than that seen in the as-machined sample, Fig. 1a. The failure initiated around the corner, Fig. 8a, propagated from grain-to-grain under stress possibly due to SCG. Finally, the crack reached a critical size

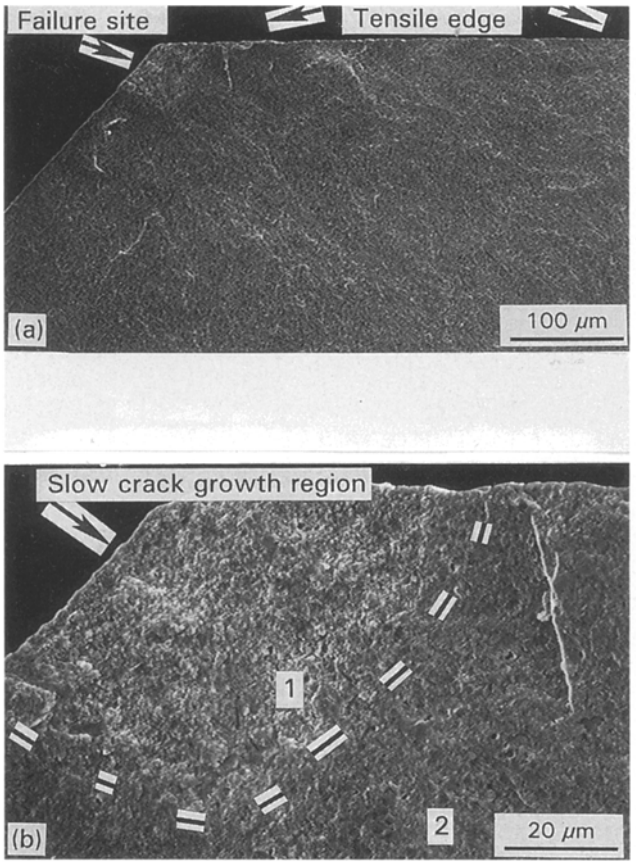

Figure 8 SEM fractographs showing (a) failure initiation, propagation and (b) formation of an SCG region in an NGK–Z-191 specimen tested in stress rupture mode at 600 °C, 344 MPa, failing at 153 h.

or formed a sufficiently larger SCG region, Fig. 8b, resulting in catastrophic failure.

As the applied stress was increased to 413 MPa, a total of four specimens were tested, two failing in short durations of 3 and 10 h, and two sustaining the stress for over 250 h, Table II, without showing bending and failure. The two specimens failing in short duration displayed two different types of "failure origin", as shown in Figs 9 and 10. However, the mechanism for final failure in both specimens was the same as discussed below. The specimen failing in 3 h is shown in Fig. 9. Examination of the fracture surface in SEM, Fig. 9a, clearly revealed a "failure initiation site" surrounded by a SCG region or "failure zone", whose boundary is indicated by dashed lines. Further examination of the failure initiation site revealed that it was a porous region, Fig. 9b, containing glassy phase silica (SiO_2) impurity, as confirmed by the energy dispersive X-ray spectra. The specimen failing in 10 h is shown in Fig. 10. Examination of the fracture surface in SEM revealed that failure initiation occurred at a large region of c-phase zirconia grains, Fig. 10b. The large size c-phase zirconia grains are weak in flexural strength [29] and easily cleave under stress. It is believed that the failure originated by transgranular cleavage of the c-phase zirconia grains, but the "flaw" was not large enough to induce catastrophic failure. Under continued stress, SCG occurred surrounding the failure initiation site, achieved a critical size (Griffth flaw), shown as "failure zone", Fig. 10a, and

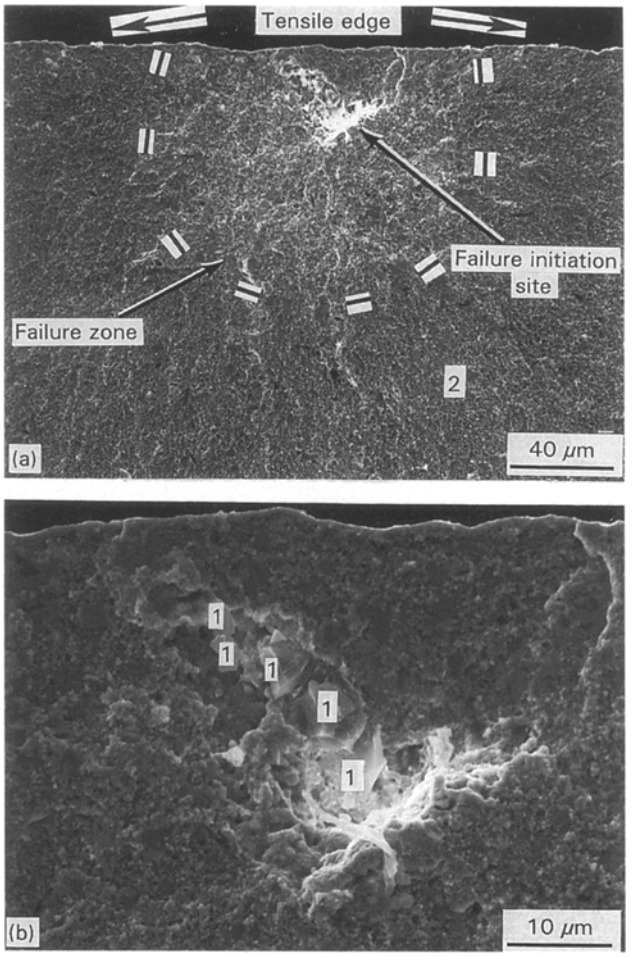

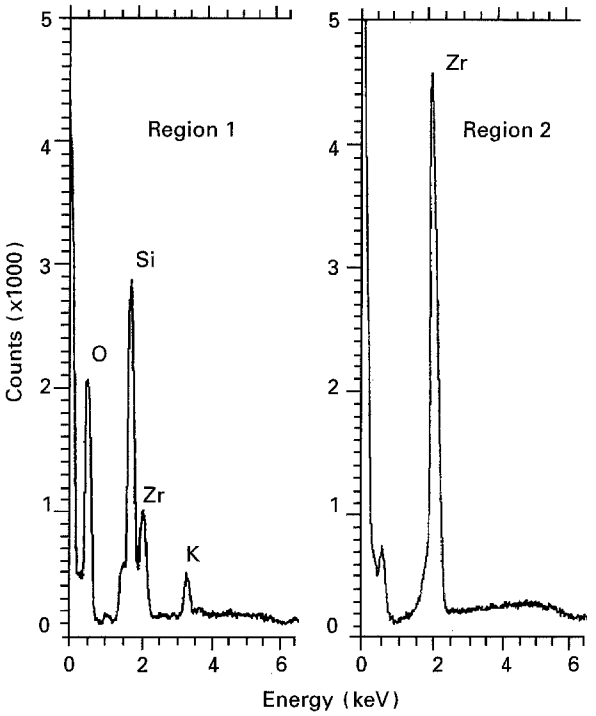

Figure 9 SEM fractographs showing (a) failure initiation at a porous region and subsequent crack growth to a critical size before final failure occurred in a stress rupture specimen (NGK–Z-191) tested at 600 °C, 413 MPa, failing in 3 h, (b) failure initiation site, (c) Energy dispersive X-ray spectra taken inside the porous region identified the presence of Si and oxygen.

led to failure. The widespread presence and formation of c-phase grains in the microstructure is indicated by small arrows, Fig. 10b. The nature of crack propagation inside (region 1) and outside (region 2) of the

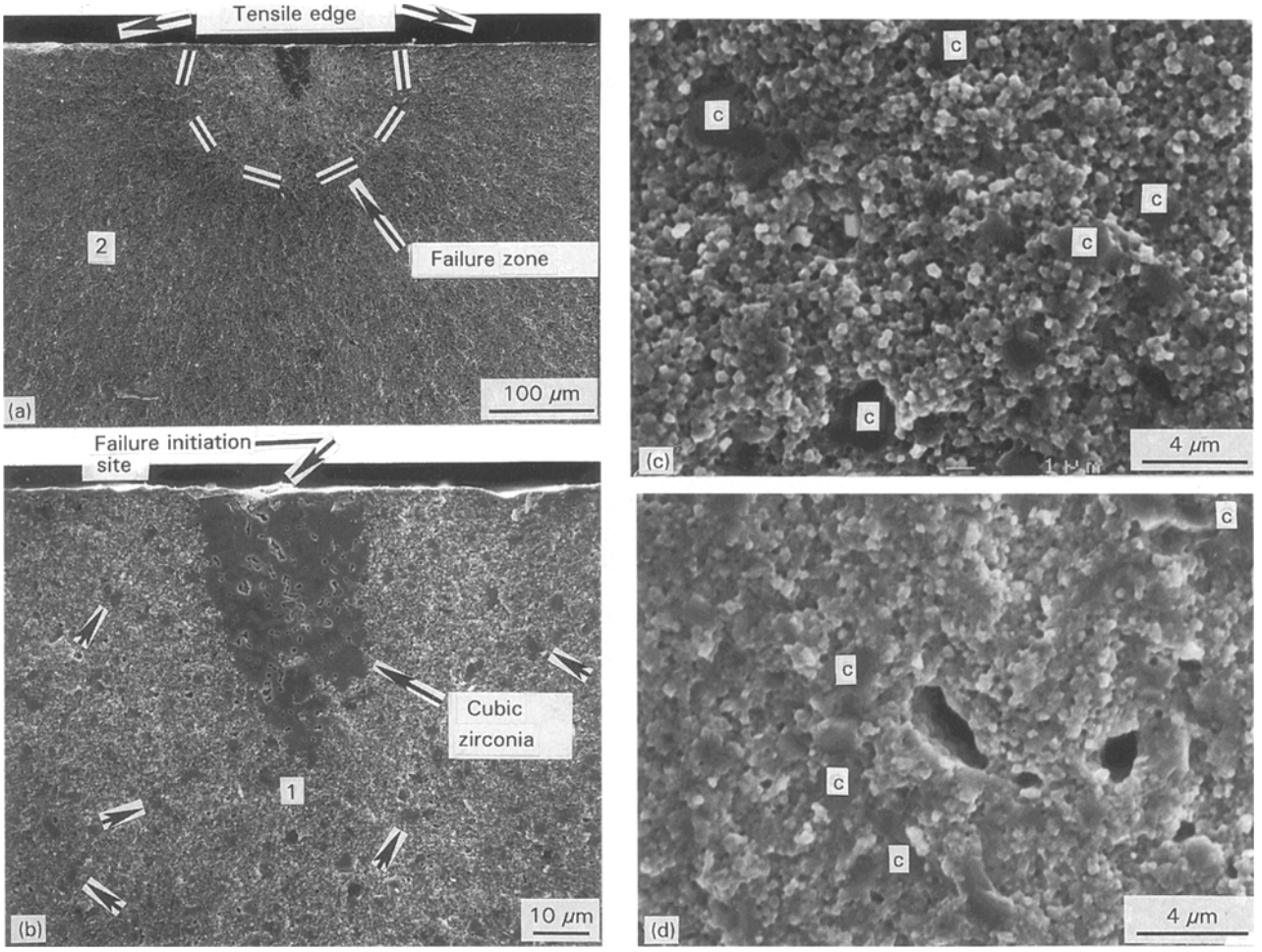

Figure 10 SEM fractographs showing (a) failure initiation at an agglomerate of large c-phase zirconia grains and (b) subsequent crack growth to a critical size before final failure occurred in a stress rupture specimen (NGK–Z-191), tested at 600 °C, 413 MPa, failing in 10 h. (c, d) show topographies of regions 1 and 2, respectively.

SCG region is revealed in Fig. 10c, d respectively. These micrographs clearly show that "slow crack growth" occurred exclusively by intergranular crack propagation, Fig. 10c, and was primarily confined to the tetragonal or monoclinic grains surrounding the failure initiation site. In the fast fracture region (outside of the "failure zone"), the crack propagation occurred exclusively transgranularly, Fig. 10d. X-ray diffraction taken from the tensile surface of the fractured specimen is shown in Fig. 1h and is similar to that seen earlier, Fig. 1g.

The other two specimens that were tested under similar conditions as the last two, but sustained the stress for over 250 h and did not show bending, clearly suggest strong variability in the size and distribution of flaws resulting from inhomogeneous composition and variability in sintering conditions.

At 800 °C, a total of five specimens were tested, Table II. At an applied stress of 344 MPa, three specimens were tested, one failing in short duration (5 h), and the other two sustaining the stress for over 200 h, and displaying minor bending. The specimen failing in 5 h, failed at the outer loading edge and the fracture surfaces failed to reveal the failure origin. The applied stress was increased to 413 MPa and two specimens were tested. One specimen failed in 11 h, displaying corner type failure, while the other specimen sustained the stress for 260 h without failure and showed minor bending.

At 1000 °C, two specimens were tested, Table II, and the material was incapable of sustaining even low magnitudes of applied stress (276 MPa) for some durable time (> 10 h).

It is important to point out that some specimens tested at relatively low temperatures, such as 200 and 400 °C, showed bending, while other specimens tested at increased temperature such as 600 °C did not show bending. This behaviour is not clearly understood and may be associated with the hydrothermal attack [53–63] of water–humidity, which is maximum in this temperature range (200–300 °C) and causes the tetragonal to monoclinic transformation. It should be noted that these tests point out the importance of stress rupture testing in showing a material's instability (degradation in strength due to either a new phase formation, microcrack initiation or creep deformation) at temperatures ranging from 200 to 1000 °C, compared to fast fracture testing (MCS = 0.5 mm min^{-1}) at similar temperatures, which failed to detect the onset of a new phase transformation/formation and creep deformation.

4. Conclusions

At room temperature, failure was primarily governed by the presence of processing defects, like porosity and large c-phase grains.

Flexural strength decreased significantly with increasing temperature, and this effect was noticeable at temperatures as low as 300 and 400 °C. Failure occurred in a brittle manner; the mode of crack propagation during fast fracture (MCS = 0.5 mm min^{-1}) was primarily transgranular up to 1000 °C.

Extensive flexural stress rupture evaluation in the temperature range 200–800 °C has identified the stress levels for time dependent failures. In addition, stress rupture testing at 600 °C and above revealed the onset of creep deformation due to viscous flow of the glassy phase and consequent degradation of the material strength.

Acknowledgements

It is a pleasure to thank colleague W. Trela for discussions and comments during testing, evaluation and writing of this paper. Thanks are due to several colleagues, especially the late C. Peters for X-ray diffraction, Y. T. Lu and Dr W. T. Donlon for SEM work.

References

1. W. BRYZIK and R. KAMO, "Tacom/Cumins Adiabatic Engine Program", in International Congress and Exposition, SAE Paper 830314 (Detroit, MI, 1983).
2. M. MARMACH, D. SERVENT, R. H. J. HANNINK, M. J. MURRAY and M. V. SWAIN, "Toughened PSZ Ceramics – Their Role as Advanced Engine Components" *ibid.* Paper 830318 (Detroit, MI, 1983).
3. M. E. WOODS, W. F. MANDLER Jr and T. L. SCOFIELD, *Ceram. Bull.* **64** (1985) 287.
4. D. W. RICHERSON, *ibid.* **64** (1985) 282.
5. R. H. J. HANNINK, M. MARMACH, M. J. MURRAY and M. V. SWAIN, in "Proceedings of the Eleventh Australian Ceramic Conference", Sydney, Australia (Australian Ceramic Society, 1984) p. 57.
6. R. STEVENS, "An Introduction to Zirconia", 2nd Edn (Magnesium Elektron Ltd, Twickenham, 1986).
7. E. M. LOGOTHETIS, in "Advances in Ceramics", Vol. 3, edited by A. H. Heuer and L. W. Hobbs (American Ceramic Society, Columbus, OH, 1981) p. 388.
8. R. C. GARVIE, C. URBANI, D. R. KENNEDY and J. C. McNEUER, *J. Mater. Sci.* **19** (1984) 3224.
9. R. C. GARVIE, in "Advances in Ceramics", Vol. 12, edited by N. Claussen, M. Ruhleand and A. H. Heuer (American Ceramic Society, Columbus, OH, 1984) pp. 465–479.
10. U. DWORAK, H. OLAPINSKI, D. FINGERLE and U. KROHN, *ibid.* pp. 480–487.
11. P. BOCH, P. FAUCHAIS, D. LOMBARD, B. ROGEAUX and M. VARDELLE, *ibid.* pp. 488–502.
12. D. S. SUHR, T. E. MITCHELL and R. J. KELLER, *ibid.* pp. 503–517.
13. F. J. ESPER, K. H. FRIESE and A. H. GEIER, *ibid.* pp. 528–536.
14. R. V. ALLEN, W. E. BORBIDGE and P. T. WHELAN, *ibid.* pp. 537–543.
15. Y. Y. WU and S. T. ZHAO, in "Third International Symposium on Ceramic Materials and Components for Engines", edited by V. J. Tennery (American Ceramic Society, Westerville, OH 1989) p. 1202.
16. P. H. RIETH, J. S. REED and A. W. NAUMANN, *Bull. Amer. Ceram. Soc.* **55** (1976) 717.
17. T. K. GUPTA, J. H. BECHTOLD, R. C. KUZNICKI, L. H. CADOFF and B. R. ROSSING, *J. Mater. Sci.* **12** (1977) 2421.
18. T. K. GUPTA, *Sci. Sint.* **10** (1978) 205.
19. T. K. GUPTA, F. F. LANGE and J. H. BECHTOLD, *J. Mater. Sci.* **13** (1978) 1464.
20. T. W. COYLE, W. S. COBLENZ and B. A. BENDER, *Amer. Ceram. Soc. Bull.* **62** (1983) 966.
21. K. TSUKUMA and M. SHIMADA, *J. Mater. Sci.* **20** (1985) 1178.
22. I. NETTLESHIP and R. STEVENS, *Int. J. High Technol. Ceram.* **3** (1987) 1.
23. F. F. LANGE, *J. Mater. Sci.* **17** (1982) 225.
24. *Idem, ibid.* **17** (1982) 235.
25. *Idem, ibid.* **17** (1982) 240.
26. I. ODA, M. MATSUI and T. SOMA, in "International Symposium on Ceramic Components for Engines" (Elsevier, London, 1986).
27. M. RUHLE and A. H. HEUER, in "Advances in Ceramics", Vol. 12, "Science and Technology of Zirconia", edited by N. Claussen, M. Ruhle and A. H. Heuer (American Ceramic Society, Columbus, OH, 1984) pp. 14–32.
28. M. RUHLE, N. CLAUSSEN and A. H. HEUER, *ibid.* pp. 352–370.
29. M. MATSUI, T. SOMA and I. ODA, *ibid.* pp. 371–381.
30. K. TSUKUMA, Y. KUBOTA and T. TSUKIDATE *ibid.* pp. 382–390.
31. H. SCHUBERT, N. CLAUSSEN and M. RUHLE, *ibid.* pp. 766–773.
32. T. K. GUPTA and C. A. ANDERSON, *Ceram. Engr. Sci. Proc.* **7** (1986) 1150.
33. C. A. ANDERSON and T. K. GUPTA, *ibid.* **7** (1986) 1158.
34. M. MATSUI, T. SOMA and I. ODA, *J. Amer. Ceram. Soc.* **69** (1986) 198.
35. F. F. LANGE, *ibid.* **69** (1986) 240.
36. T. MASAKI, *ibid.* **69** (1986) 638.
37. L. J. SCHIOLER, "Effect of Time and Temperature on Transformation Toughened Zirconias", Technical Report TR 87–29, US Army Materials Technology Laboratory, Watertown, MA, June 1987.
38. J. J. SWAB, "Properties of Yttria-Tetragonal Zirconia Polycrystal (Y–TZP) Materials After Long-Term Exposure to Elevated Temperatures", Technical Report TR 89-21, US Army Materials Technology Laboratory, Watertown, MA, March 1989.
39. J. SUNG and P. S. NICHOLSON, *J. Amer. Ceram. Soc.* **71** (1988) 788.
40. K. NOGUCHI, Y. MATSUDA, M. OISHI, T. MASAKI, S. NAKAYAMA and M. MIZUSHINA, *ibid.* **73** (1990) 2667.
41. R. K. GOVILA, Technical Report TR 80-18 (Army Materials and Mechanics Research Center, Watertown, MA, May 1980).
42. R. K. GOVILA, J. A. HERMAN and N. ARNON, ASME Paper No. 85-GT-181, Gas Turbine Conference, Houston, TX, 18–21 March, 1985.
43. R. K. GOVILA, *J. Mater. Sci.* **26** (1991) 1545.
44. D. J. CASSIDY, R. L. VAN ALSTEN and M. E. MILBERG, US Patent No. 4866014, 12 September 1989.
45. NGK INSULATORS, Ltd, Nagoya, "Properties of Zirconia" (1984).
46. D. C. LARSEN and J. W. ADAMS, "Long-Term Stability and Properties of Zirconia Ceramics for Heavy Duty Diesel Engine Components", NASA Lewis Research Center, Cleveland, OH, US Department of Energy, Contract DEN 3-305 NASA CR-174943 (1985).
47. N. L. HECHT, D. E. McCULLUM, D. W. GRANT, J. D. WOLF, G. A. GRAVES and S. M. GOODRICH, "The Experimental Evaluation of Environmental Effects in Toughened Ceramic for Advanced Heat Engines", in "Proceedings of the 24th Automotive Technology Development Contractors Coordination Meeting" (SAE, Warrendale, PA, 1987) pp. 209–222.
48. P. LINTULA, T. LEPISTO, E. LEVANEN, T. MANTYLA and L. LEPISTO, *Ceram. Eng. Sci. Proc.* **9** (1988) 1279.
49. N. L. HECHT, S. M. GOODRICH, D. E. McCULLUM, P. P. YANEY, S. D. JANG and V. J. TENNERY, *Amer. Ceram. Soc. Bull.* **71** (1992) 955.
50. D. B. MARSHALL, *J. Amer. Ceram. Soc.* **69** (1986) 173.
51. M. L. MECARTNEY, *ibid.* **70** (1987) 54.
52. J. DRENNAN and R. H. J. HANNINK, *ibid.* **69** (1986) 541.
53. K. KOBAYASHI, H. KUWAJIMA and T. MASAKI, *Solid State Ionics* **3** (1981) 489.

54. M. WATANABE, S. ITO and I. FUKUURA, in "Advances in Ceramics, Science and Technology of Zirconia II", Vol. 12, edited by N. Claussen, M. Ruhle and A. H. Heuer (American Ceramic Society, Columbus, OH, 1984) pp. 391–398.
55. K. NAKAJIMA, K. KOBAYASHI and Y. MURATA, *ibid.* pp. 399–407.
56. T. SATO and M. SHIMADA, *J. Amer. Ceram. Soc.* **67** (1984) C212.
57. *Idem, ibid.* **68** (1985) 356.
58. T. SATO, S. OHTAKI and M. SHIMADA, *J. Mater. Sci.* **20** (1985) 1466.
59. K. TSUKAMA and M. SHIMADA, *J. Mater. Sci. Lett.* **4** (1985) 857.
60. M. YOSHIMURA, T. NOMA, K. KAWABATA and S. SOMIYA, *ibid.* **6** (1987) 465.
61. F. F. LANGE, G. L. DUNLOP and B. I. DAVIS, *J. Amer. Ceram. Soc.* **69** (1986) 237.
62. S. Y. CHEN and H. Y. LU, *J. Mater. Sci.* **24** (1989) 453.
63. J. J. SWAB, *ibid.* **26** (1991) 6706.

Received 31 January
and accepted 6 July 1994